

ORIGINAL ARTICLE

Open Access



Analysis of the gain factors of 5G-assisted BDS RTK positioning in urban environments

Weixiang Chen¹, Tengfei Wang^{1*} , Zheng Yao¹, Mingquan Lu¹, Yi Wang² and Cheng Li²

Abstract

The joint utilization of the Fifth Generation Communications Technology (5G) and the Global Navigation Satellite System (GNSS) serves as a promising solution to address the challenges associated with insufficient visible satellites and lower observation quality in urban environments. 5G allows for the angle and distance measurements, augmenting the performance of Real-Time Kinematic (RTK) positioning. To quantify the improvement of 5G observations on RTK positioning, this paper proposes a float solution gain factor and the Ambiguity Dilution of Precision (ADOP) gain factor. Based on these gain factors, the theoretical analysis and simulation are performed. This study designs an extended Kalman filter for 5G-assisted BeiDou Navigation Satellite System (BDS) RTK positioning, employing both the Full Ambiguity Resolution (FAR) and Partial Ambiguity Resolution (PAR) modes. Our experiment verified the effectiveness of 5G-assisted BDS RTK positioning in mitigating outlier occurrences and improving the ambiguity fixing rate as well as the positioning accuracy. In the FAR and PAR modes, the Three-Dimensional (3D) spatial accuracy increased by 48% and 18.8%, respectively, and the results are consistent with theoretical analysis based on gain factors. The fixing rate of RTK increased from 11.11% to 13.93%, while it increased from 32.58% to 44.43% for the PAR mode. The assistance of 5G observations reduced the median error for the FAR mode from over 1.3m to 0.9 m, and the third quartile from 2.1m to 1.05 m. For the PAR mode, the median error decreased from 0.5m to 0.12 m, and the third and fourth quartiles decreased from 0.65m to 0.38 m.

Keywords BeiDou Navigation Satellite System (BDS), Fifth Generation Communications Technology (5G), Real-time kinematic (RTK), Hybrid positioning

Introduction

High-accuracy positioning in complicated urban environments is becoming increasingly important, which plays a crucial role in people's daily life, public services, and emerging unmanned systems, especially in the booming development of the Internet of Things (IoT) industry (Moradbeikie et al., 2021; Takikawa et al., 2021; Yu et al., 2014; Zangenehjad and Gao, 2021). To achieve high-precision positioning, Real-Time Kinematic

(RTK) positioning is extensively utilized, wherein Global Navigation Satellite System (GNSS) observations are simultaneously collected by a stationary base station and a rover. However, the performance of RTK in dense urban environments fails to satisfy the stringent precision demands of numerous dynamic systems. The frequent signal obstruction in dynamic scenarios results in a reduction in the number of observable satellites (Medina et al., 2021), and the observation quality is degraded by multipath errors induced by trees and tall structures (Bai et al., 2020), consequently leading to a sharp decline in the ambiguity fixing rate and positioning accuracy (Medina et al., 2021).

There is increasing attention to integrating GNSS with diverse wireless systems, including Wi-Fi, Bluetooth, Ultra-Wideband (UWB), and cellular signals. The

*Correspondence:

Tengfei Wang
tfee@tsinghua.edu.cn

¹ Department of Electronic Engineering, Tsinghua University, Beijing 100000, China

² Huawei Technologies Co., Ltd., Shanghai 200000, China

combined use of wireless systems can alleviate the GNSS degradation arising from the obstructions and interference of satellite signals. Among the above systems, the Fifth Generation Communications Technology (5G) cellular signal has attracted a widespread attention due to its superior speed, higher bandwidth, and deployment density.

The 5G mobile networks have offered alternative positioning resources in urban environments. Cellular systems are widely recognized for their communication advantages, and 5G cellular systems, in particular, harness key enabling technologies such as smaller cells, higher carrier frequencies, and Multiple-Input Multiple-Output (MIMO) (Keating et al., 2019), have the capability for meter-level positioning accuracy. Currently, 5G cellular positioning technology can be categorized into four main classifications: identity recognition, signal fingerprinting, angle measurement, and ranging.

1. Location determination based on Cell Identity (CID) involves monitoring whether the target device is within the coverage area of the base stations (Li et al., 2022). The precision of CID method is constrained by the density of base station deployment, exhibiting significantly lower precision compared to other technologies.
2. Fingerprint-based positioning methods collect the features such as signal strength and delay to establish a fingerprint database and compare the features of the received signals with the database to achieve positioning (Wang et al., 2023).
3. Positioning utilizing angles involves the use of the Angle of Arrival (AoA), Angle of Departure (AoD), or a combination of both for localization. The 5G network incorporates MIMO techniques, and the base stations equipped with hundreds or even thousands of antenna elements can form a large antenna array, enabling efficient beamforming (Shahmansoori et al., 2018). Beamforming not only provides AoD information regarding the UE position based on the beam ID accessed by the UE but also enhances the Signal-to-Noise Ratio (SNR) due to beamforming gain. Therefore, the AoD and AoA can provide precise angle information in 5G system.
4. Time of Arrival (TOA) (Deng et al., 2020), Time Difference of Arrival (TDOA) (Pan et al., 2022), and Round Trip Time (RTT) (Del Peral-Rosado et al., 2020) have become prevalent distance measurement techniques in mobile networks. However, precision TOA ranging requires strict time synchronization between the user and the base station, and TDOA depends on the time difference in signal transmission among multiple base stations. To improve the

ranging ability of cellular system, the list of supported ranging methods has expanded to include RTT in 5G. This relative time measurement enables RTT ranging to better overcome the impact of time synchronization errors, thereby enhancing the precision and reliability of positioning.

Currently, 5G base stations have been extensively deployed, particularly in urban environments, and the positioning accuracy based on RTT and AoA can achieve sub-meter level. Therefore, in urban environments, the combination of GNSS and 5G can enhance the precision of RTK positioning and improve the fixing rate in ambiguity resolution.

The positioning using both GNSS and 5G has attracted increasing attention. Some scholars analyzed the performance gains due to an integration of GNSS and 5G (Destino et al., 2018; Abu-Shaban et al., 2020). Their work focuses on analyzing the performance boundaries of GNSS and 5G fusion. Del Peral-Rosado et al. (2018) further proposed a model of GNSS+5G and conducted low-complexity simulations which only used 5G DL-TDoA measurements to achieve single epoch positioning. Wang et al. (2022) adopted a tightly coupled Kalman federated filter and demonstrated through simulations and experiments that the addition of 5G ranging significantly improved the accuracy of the INS/GNSS integrated positioning. Li et al. (2022) simulated different satellite obstruction environments to analyze the influences of the number of base stations, geometric configuration, etc., on the performance of fusion positioning with 5G ranging and BDS.

However, based on our limited knowledge, the focus of 5G-assisted GNSS positioning lies in the integration of 5G observations and pseudorange (Bai et al., 2022; Destino et al., 2018; Abu-Shaban et al., 2020). While some studies also involve the fusion of 5G observations and RTK positioning (Li et al., 2023; Zheng et al., 2023), there is still a lack of theoretical analysis and real-world experimental validation for the performance gains of 5G-assisted RTK. In this study, we propose two gain factors to quantitatively analyze the improvement brought by 5G observations on RTK positioning. In experimental validation, we propose a 5G-assisted BDS RTK positioning approach, which integrates the Extended Kalman Filter (EKF) and ambiguity resolution based on Least-squares Ambiguity Decorrelation Adjustment (LAMBDA).

The core contributions are as follows:

1. Based on double difference observations and 5G observation models, we derive the Cramer–Rao Lower Bound (CRLB) of user position and double

difference ambiguities, proving the enhancement of 5G RTT and AoA observations on estimation accuracy of float solution and Ambiguity Dilution of Precision (ADOP). Furthermore, we propose gain factors to quantify the improvement brought by 5G observations.

2. We statistically analysis 5G angle measurement accuracy in a dynamic environment based on the data recorded at actual 5G base stations and by Customer Premises Equipment (CPE).
3. We implemented real-world experiments to compare RTK positioning results in BDS only case and BDS/5G case, demonstrating the advantages of proposed method in practice.

The subsequent sections of this paper are structured as follows. In Sect. [Measurements and positioning algorithm](#), an overview of the observation modelling for both BDS and 5G systems is presented. Section [Performance analysis of BDS/5G RTK solution](#) introduces a 5G-assisted BDS RTK positioning method based on EKF and LAMBDA. The theoretical gains of single-station 5G-assisted BDS RTK are analyzed and quantified in Sect. [Simulation](#). Section [Experiment and results analysis](#) presents the gain factors and validates the advantages of proposed method by numerical simulations. In Sect. [Experiment and results analysis](#), real-world positioning experiments verify the performance improvements of the proposed method.

Measurements and positioning algorithm

We consider a 5G-assisted BDS RTK positioning presented in Fig. 1. The scenario encompasses a single 5G base station and M visible satellites. The user's position is denoted as $\mathbf{p}_r = (x_r \ y_r \ z_r)^T$, and the positions of the i -th satellite as $\mathbf{p}_s^i = (x_s^i \ y_s^i \ z_s^i)^T$. The location of the 5G base station is denoted as $\mathbf{p}_{BS} = (x_{BS} \ y_{BS} \ z_{BS})^T$.

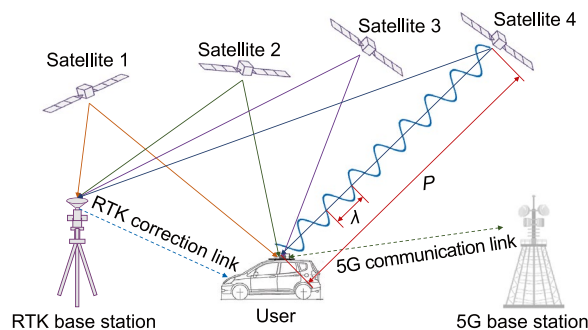


Fig. 1 Concept of the 5G-assisted BDS RTK positioning system

BDS measurements

RTK positioning is an widely used technique and can achieve centimeter-level positioning accuracy. RTK corrects the errors in GNSS measurements by Double Difference (DD) operations. It involves differencing the measurements between two receivers to remove common errors such as satellite clock errors and atmospheric delays. BDS DD measurement vector is written as:

$$\mathbf{y}_{BDS} = (\mathbf{P}^T \ \mathbf{L}^T)^T \tag{1}$$

where \mathbf{P} and \mathbf{L} denote DD pseudorange and DD carrier phase vector, respectively. Equation (2) gives the DD pseudorange and DD carrier phase measurement models in a short baseline condition.

$$\begin{aligned} \nabla \Delta P_{rb,f}^{(ki)} &= \nabla \Delta \rho_{rb}^{(ki)} + \varepsilon_{P,rb}^{(ki)} \\ \nabla \Delta L_{rb,f}^{(ki)} &= \nabla \Delta \rho_{rb}^{(ki)} - \lambda_f \nabla \Delta N_{rb,f}^{(ki)} + \varepsilon_{L,rb}^{(ki)} \end{aligned} \tag{2}$$

Here, $\nabla \Delta(\cdot)$ operator refers to the DD operation on raw pseudorange or raw carrier phase. Raw observations can be formulated as:

$$\begin{aligned} P_{r,f}^{(i)} &= \rho_r^{(i)} + c(\delta t_r - \delta t_i) + I_{r,f}^{(i)} + T_r^{(i)} + \varepsilon_{iP} \\ L_{r,f}^{(i)} &= \rho_r^{(i)} + c(\delta t_r - \delta t_i) - I_{r,f}^{(i)} + T_r^{(i)} + \lambda_f N_{r,f}^{(i)} + \varepsilon_{iL} \end{aligned} \tag{3}$$

where, $\rho_r^{(i)} = \|\mathbf{p}_r - \mathbf{p}_s^{(i)}\|$ denotes the distance from the rover to satellite i , c represents the speed of light, λ_f denotes the wavelength at the f -th frequency, δt_r and δt_i denote the clock bias of rover and satellite i , respectively, $I_{r,f}^{(i)}$ represent ionospheric delay, $T_r^{(i)}$ denotes tropospheric delay, $N_{r,f}^{(i)}$ represents the ambiguity, $\varepsilon_{iP} \sim \mathcal{N}(0, \sigma_{iP}^2)$ and $\varepsilon_{iL} \sim \mathcal{N}(0, \sigma_{iL}^2)$ denote measurement errors for pseudorange and carrier phase observations, respectively.

In this paper, we adopt the elevation-based noise model, which is widely used in GNSS software (Takasu, 2013; King, 1995; Chen et al., 2021):

$$\begin{aligned} \sigma_{iP}^2 &= F^2(a^2 + b^2 \sin^2 \theta_i) \\ \sigma_{iL}^2 &= (a^2 + b^2 \sin^2 \theta_i) \end{aligned} \tag{4}$$

where a and b are base term and elevation factor, respectively, with both assigned a value of 0.003, θ_i is the i -th satellite elevation, and F is the code/carrier-phase error ratio which is set to 100. The parameter settings are based on the default noise parameter settings in software configuration (Takasu, 2013; Chen et al., 2021).

Equation (5) is the auto-covariance matrix of DD noise vector:

$$\mathbf{R}_{BDS} = \begin{pmatrix} \mathbf{R}_{L,DD} & \\ & \mathbf{R}_{P,DD} \end{pmatrix} \quad (5)$$

In equation (5), $\mathbf{R}_{L,DD}$ and $\mathbf{R}_{P,DD}$ stand for auto-covariance matrix of DD carrier phase noise and DD pseudorange noise, which can be calculated by raw measurement noise in equation (4). The propagation of noise from raw measurement to DD measurement is the fundamental operation in RTK, whose comprehensive descriptions are provided in the pertinent literature (Liu et al., 2016).

5G measurement

In our method, in addition to BDS measurements, 5G provides the ranging and angle measurements between base station and users, which is illustrated in Fig. 2. The measurement vector of 5G system is expressed as:

$$\mathbf{y}_{5G} = (d \ \alpha \ \beta)^T \quad (6)$$

where d denotes RTT ranging, α and β present azimuth AoA and zenith AoA respectively.

The representation of RTT distance measurement is as follows:

$$d = \left(\frac{t_{\text{up-link}} + t_{\text{down-link}}}{2} \right) \cdot c = \|\mathbf{p}_r - \mathbf{p}_{BS}\| + \varepsilon_d \quad (7)$$

where $t_{\text{up-link}}$ and $t_{\text{down-link}}$ denote the up-link delay and the down-link delay, $\varepsilon_d \sim \mathcal{N}(0, \sigma_d^2)$ denotes ranging error mainly from propagation delay and clock drift.

In Fig. 2, a substantial number of antennas on the receiver in the uplink can accomplish precise AoA measurements. These measurements allow for the determination of both the azimuth AoA and the zenith AoA of the user signal on the antenna array. The detailed mathematical derivation for calculating the AoA based on the electromagnetic signals received by the antennas can be found in (Xhafa et al., 2021).

Angular measurement can be formulated as:

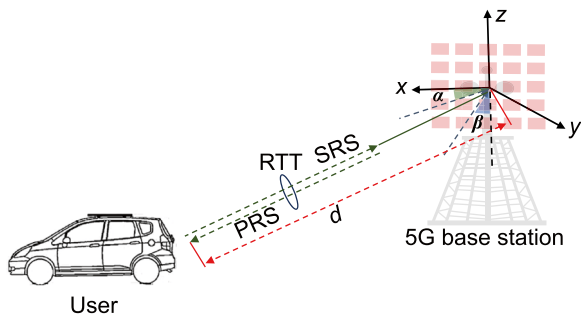


Fig. 2 Illustration of 5G measurements

$$\alpha = \arctan \left(\frac{y_r - y_{BS}}{x_r - x_{BS}} \right) + \varepsilon_\alpha \quad (8)$$

$$\beta = \arccos \left(\frac{z_r - z_{BS}}{\|\mathbf{p}_r - \mathbf{p}_{BS}\|} \right) + \varepsilon_\beta$$

where $\varepsilon_\alpha \sim \mathcal{N}(0, \sigma_\alpha^2), \varepsilon_\beta \sim \mathcal{N}(0, \sigma_\beta^2)$ represent AoA measurement error and ZoA measurement.

Therefore, for the observation vector in equation (6), the expression for the auto-covariance of noise vector is denoted as:

$$\mathbf{R}_{5G} = \text{diag}(\sigma_d^2, \sigma_\alpha^2, \sigma_\beta^2) \quad (9)$$

BDS/5G RTK positioning algorithm

The approach proposed in this paper utilizes 5G AoA measurements and RTT ranging to assist BDS RTK positioning. We employ EKF to achieve a float solution and then conducts ambiguity resolution and validation based on the float solution and its covariance. Baseline will be updated ultimately according to integer ambiguity to achieve high precision positioning. The flowchart of proposed algorithm is illustrated in Fig. 3.

State update

The state transition equation of the EKF employed in this work is presented as follows:

$$\mathbf{x}_k = \mathbf{F}_k \mathbf{x}_{k-1} + \boldsymbol{\omega}_k \quad (10)$$

where $\mathbf{x}_k \in \mathbb{R}^n$ is the underlying state vector, \mathbf{F}_k is one-step transition matrix, and $\boldsymbol{\omega}_k$ represents the process noise.

We use Constant Position (CP) model for the receivers with low-dynamic motion. The method proposed can be easily extended to other motion models. In the CP model, the state vector can be expressed as follows:

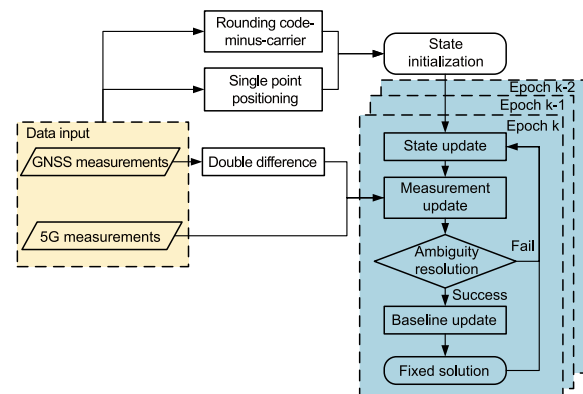


Fig. 3 Flowchart of proposed method

$$\mathbf{x}_k = \begin{pmatrix} \mathbf{p}_{r,k}^T & \mathbf{a}_k^T \end{pmatrix} \quad (11)$$

where $\mathbf{p}_{r,k} = (x_{r,k} \ y_{r,k} \ z_{r,k})^T$ denotes the position vector of the rover in the k -th epoch, and $\mathbf{a}_k = (\Delta N_{rb,1}^{(1)} \ \dots \ \Delta N_{rb,1}^{(M)} \ \Delta N_{rb,2}^{(1)} \ \dots \ \Delta N_{rb,2}^{(M)})$ signifies single difference ambiguity vector in the k -th epoch.

One-step state transition matrix \mathbf{F}_k is formulated as:

$$\mathbf{F}_k = \begin{pmatrix} \mathbf{I}_{3 \times 3} & \mathbf{0}_{3 \times 2M} \\ \mathbf{0}_{2M \times 3} & \mathbf{I}_{2M \times 2M} \end{pmatrix} \quad (12)$$

System noise matrix \mathbf{Q}_k is formulated as:

$$\mathbf{Q}_k = \begin{pmatrix} \infty_{3 \times 3} & \mathbf{0}_{3 \times 2M} \\ \mathbf{0}_{2M \times 3} & \mathbf{0}_{2M \times 2M} \end{pmatrix} \quad (13)$$

To reduce reliance on the receiver's dynamic situation, the above position-related items are set as infinity symbol, while ambiguity terms are set to zero due to their time invariance.

The initial values of position is given by Single Point Positioning (SPP), while those ambiguities are estimated by rounding code-minus-carrier (Xie, 2009).

One-step state transition matrix and its covariance matrix in the EKF are presented as follows:

$$\begin{cases} \mathbf{x}_{k+1|k} = \mathbf{F}_{k+1} \mathbf{x}_k \\ \mathbf{P}_{k+1|k} = \mathbf{F}_{k+1} \mathbf{P}_k \mathbf{F}_{k+1}^T + \mathbf{Q}_k \end{cases} \quad (14)$$

Measurement update

Both BDS and 5G measurements are modeled as nonlinear functions. Their measurement equations can be formulated as a nonlinear function as follow:

$$\mathbf{y}_k = h(\mathbf{x}_k) + \mathbf{v}_k \quad (15)$$

The non-linear function $h(\cdot)$ as given in equation (15) represents the relationship between the measurements \mathbf{y}_k and the states \mathbf{x}_k , which is given by (3)(7)(8), and \mathbf{v}_k is the measurement noise.

$$\mathbf{y}_k = (\mathbf{y}_{\text{BDS}}^T \ \mathbf{y}_{5G}^T)^T \quad (16)$$

The measurement update in EKF can be formulated as:

$$\begin{cases} \mathbf{K}_{k+1} = \mathbf{P}_{k+1|k} \mathbf{H}_{k+1}^T (\mathbf{H}_{k+1} \mathbf{P}_{k+1|k} \mathbf{H}_{k+1}^T + \mathbf{R}_{k+1})^{-1} \\ \mathbf{x}_{k+1} = \mathbf{x}_{k+1|k} + \mathbf{K}_{k+1} (\mathbf{y}_{k+1} - h(\mathbf{x}_{k+1|k})) \\ \mathbf{P}_{k+1} = (\mathbf{I} - \mathbf{K}_{k+1} \mathbf{H}_{k+1}) \mathbf{P}_{k+1|k} \end{cases} \quad (17)$$

The prior covariance matrix $\mathbf{P}_{k+1|k}$ is applied to calculate filtering gains \mathbf{K}_{k+1} and then update the covariance matrix \mathbf{P}_{k+1} . The Jacobian matrix \mathbf{H}_{k+1} is shown as:

$$\mathbf{H}_{k+1} = \frac{\partial \mathbf{y}_{k+1}}{\partial \mathbf{x}_{k+1}} = \begin{pmatrix} \mathbf{G} & \lambda_1 \mathbf{D} & \mathbf{0} \\ \mathbf{G} & \mathbf{0} & \lambda_2 \mathbf{D} \\ \mathbf{G} & \mathbf{0} & \mathbf{0} \\ \mathbf{G} & \mathbf{0} & \mathbf{0} \\ \mathbf{H}_{5G} & \mathbf{0} & \mathbf{0} \end{pmatrix} \quad (18)$$

where \mathbf{G} is the geometry matrix of the rover, λ_1, λ_2 represent the wavelengths corresponding to two respective frequencies, \mathbf{D} is single difference to double difference transformation matrix, its formulation can be found in reference (Zhao et al., 2023), and \mathbf{H}_{5G} is the Jacobian matrix of 5G observation.

$$\mathbf{H}_{5G} = \begin{pmatrix} \frac{x_r - x_{\text{BS}}}{\rho} & \frac{y_r - y_{\text{BS}}}{\rho} & \frac{z_r - z_{\text{BS}}}{\rho} \\ \frac{y_{\text{BS}} - y_r}{r^2} & \frac{x_r - x_{\text{BS}}}{r^2} & \mathbf{0} \\ \frac{-(x_r - x_{\text{BS}})(z_r - z_{\text{BS}})}{\rho^2 r} & \frac{-(y_r - y_{\text{BS}})(z_r - z_{\text{BS}})}{\rho^2 r} & \frac{(z_r - z_{\text{BS}})^2 + \rho^2}{\rho^2 r} \end{pmatrix} \quad (19)$$

where $r = \sqrt{(x_r - x_{\text{BS}})^2 + (y_r - y_{\text{BS}})^2}$, $\rho = \|\mathbf{p}_r - \mathbf{p}_{\text{BS}}\|$.

The measurement noise matrix of the fusion system composed BDS measurement noise matrix (5) and 5G measurement noise matrix(9).

$$\mathbf{R}_k = \begin{pmatrix} \mathbf{R}_{\text{BDS}} & \\ & \mathbf{R}_{5G} \end{pmatrix} \quad (20)$$

The state vector of proposed EKF (11) contain the Single Difference (SD) ambiguity of the i -th satellite, $\Delta N_{rb,1}^i$, and $\Delta N_{rb,2}^i$. As an example, considering the first frequency, the double difference ambiguity is obtained by differencing the SD ambiguities between satellite i and the reference satellite k .

$$\nabla \Delta N_{rb,1}^{ki} = \Delta N_{rb,1}^k - \Delta N_{rb,1}^i \quad (21)$$

The vector $\hat{\mathbf{N}}$ is constituted by all of the float DD ambiguity, and the DD ambiguity vector can be expressed as a linear transformation of SD ambiguity vector:

$$\hat{\mathbf{N}} = \text{diag}(\lambda_1 \mathbf{D}, \lambda_2 \mathbf{D}) \mathbf{a} \quad (22)$$

To express the covariance matrix of $\hat{\mathbf{N}}$, the covariance matrix \mathbf{P}_{k+1} in (17) can be expanded as:

$$\mathbf{P}_{k+1} = \begin{pmatrix} \mathbf{Q}_{\hat{p}\hat{p}} & \mathbf{Q}_{\hat{p}\hat{a}} \\ \mathbf{Q}_{\hat{a}\hat{p}} & \mathbf{Q}_{\hat{a}\hat{a}} \end{pmatrix} \quad (23)$$

The covariance matrix of DD ambiguities and SD ambiguities adheres to the principle of error propagation:

$$\mathbf{Q}_{\hat{\mathbf{N}}} = \text{diag}(\lambda_1 \mathbf{D}, \lambda_2 \mathbf{D})^T \cdot \mathbf{Q}_{\hat{a}\hat{a}} \cdot \text{diag}(\lambda_1 \mathbf{D}, \lambda_2 \mathbf{D}) \quad (24)$$

Ambiguity resolution

To obtain high accuracy positioning, after the float solution in EKF, the LAMBDA is used for ambiguity resolution, which essentially deals with the following mathematical problem:

$$\min \|N - \hat{N}\|_{Q_{\hat{N}}}^2 = (N - \hat{N})^T Q_{\hat{N}}^{-1} (N - \hat{N}) \quad (25)$$

where \hat{N} , $Q_{\hat{N}}$ represent the float solution vector of DD ambiguity and its covariance matrix.

The LAMBDA method consists of two steps: implementing Z transformation to decorrelate the ambiguities, and searching the integer vector in the solution space.

The specific methods for decorrelation have been extensively studied (Teunissen, 1993). Full Ambiguities Resolution (FAR) and Partial Ambiguities Resolution (PAR) are two commonly used search strategies.

In FAR, all components in \hat{N} will be included in searching to resolve each ambiguity. The search space can be expressed as an ellipse:

$$(\hat{N} - N^T) Q_{\hat{N}}^{-1} (\hat{N} - N) \leq \chi^2 \quad (26)$$

where χ represents the radius of the elliptical region. To ensure the reliability of result in FAR, a simple but efficient method is to employ the ratio test for validation:

$$R = \frac{(N_2 - \hat{N})^T Q_{\hat{N}}^{-1} (N_2 - \hat{N})}{(N_1 - \hat{N})^T Q_{\hat{N}}^{-1} (N_1 - \hat{N})} > R_{\text{thres}} \quad (27)$$

The variable N_1 denotes the optimal outcome obtained from the integer search, while N_2 signifies a sub-optimal result from the same search. The parameter R_{thres} defines the threshold for the Ratio Test, conventionally a value of 3 is used.

The satellites with low elevation may experience significant atmospheric delays and multipath effects, especially in urban environment, making it difficult to fix all ambiguities. PAR demonstrates the effectiveness in resolving ambiguity subset and would be a viable choice in practical scenarios (Teunissen et al., 1999; Li et al., 2014). In PAR, the vector representing the ambiguities of float solution is expressed as:

$$\hat{N} = (\hat{N}_{(j)} \hat{N}_{(M-j-1)}) \quad (28)$$

where $\hat{N}_{(j)}$ shows the subset of ambiguities, which are easy to be fixed, and $\hat{N}_{(M-j-1)}$ is the rest part which seems more difficult to be fixed. The subset $\hat{N}_{(j)}$ is selected with different heuristic criteria, such as signal-to-noise ratio (Parkins, 2011), ambiguity resolution factor (Teunissen and Odijk, 1997), or minimum deviation (Henkel and Günther, 2010). After the selection of

the subset N is completed $\hat{N}_{(j)}$, the search space will be reduced to:

$$(\hat{N}_{(j)} - N_{(j)})^T Q_{\hat{N}_{(j)}}^{-1} (\hat{N}_{(j)} - N_{(j)}) \leq \chi_{(j)}^2 \quad (29)$$

$Q_{\hat{N}_{(j)}}^{-1}$ represents the covariance matrix of the corresponding subset. The PAR method effectively reduces the search space for ambiguity, and the results from reference (Castro-Arvizu et al., 2021) indicate that the PAR mode receiver demonstrates better performance than the FAR mode in the some conditions.

Whether the integer set N is obtained through FAR or PAR, the position of float solution \hat{p}_r can be updated using the following method:

$$\check{p}_r = \hat{p}_r - Q_{\hat{p}_a} Q_a^{-1} (\hat{N} - \check{N}) \quad (30)$$

Performance analysis of BDS/5G RTK solution

This section theoretically analyzes the performance gains of BDS/5G RTK positioning. To simplify the mathematical derivation, we rewrite the expression of BDS measurements in a single frequency form. The LAMBDA method implements the resolves of DD ambiguities based on its covariance matrix. In the theoretical analysis, the vector to be estimated include rover position and DD ambiguities:

$$x = \begin{pmatrix} x_r & y_r & z_r & \nabla \Delta N_{rb}^{(k1)} & \dots & \nabla \Delta N_{rb}^{(kM)} \end{pmatrix}^T = \begin{pmatrix} p_r^T & N^T \end{pmatrix}^T \quad (31)$$

In the following, we derive CRLB for the vector in equation (31) to analyze the positioning performance. We compare the CRLB in BDS only and BDS/5G methods, and demonstrate the gains got with the 5G observations in hybrid positioning.

Gains in float solution

In equation (31), the CRLB of i -th parameter can be formulated as:

$$\sigma_{\hat{x}_i}^2 = [\mathcal{F}(\hat{x})]_{i,i}^{-1} \quad (32)$$

where $\mathcal{F}(\hat{x})$ is Fisher Information Matrix (FIM).

The measurement vector in BDS only case is given by (1), while that in BDS/5G case is given by (16). The FIM for the vector of unknown parameters are denoted as \mathcal{F}_{BDS} for BDS case and \mathcal{F}_{aid} for the BDS/5G case.

$$\mathcal{F}_{\text{BDS}} = H'_{\text{BDS}} R_{\text{BDS}}^{-1} H'_{\text{BDS}}{}^T \quad \mathcal{F}_{\text{aid}} = H' R^{-1} H'^T \quad (33)$$

R_{BDS} , R represent measurement noise matrix which can be found in (5) and (20). H'_{BDS} and H' denote the matrix

of partial derivatives, and the gradient of the measurement vector with respect to estimated vector.

$$H'_{\text{BDS}} = \begin{pmatrix} \mathbf{G} & \mathbf{\Lambda} \\ \mathbf{G} & \mathbf{0} \end{pmatrix}, H' = \begin{pmatrix} \mathbf{G} & \mathbf{\Lambda} \\ \mathbf{G} & \mathbf{0} \\ H_{5G} & \mathbf{0} \end{pmatrix} \quad (34)$$

The wavelength constant matrix is shown as $\mathbf{\Lambda} = \text{diag}(\lambda, \dots, \lambda)$.

Substitute the equation into (33) and obtain the covariance of estimated vector by taking the inverse of their FIM.

$$\begin{aligned} \mathcal{F}_{\text{BDS}}^{-1} &= \begin{pmatrix} \mathbf{Q}_{\hat{p}\hat{p}\text{BDS}} & \mathbf{Q}_{\hat{p}\hat{N}\text{BDS}} \\ \mathbf{Q}_{\hat{N}\hat{p}\text{BDS}} & \mathbf{Q}_{\hat{N}\hat{N}\text{BDS}} \end{pmatrix} \\ &= \begin{pmatrix} \mathbf{G}^T(\mathbf{R}_{\text{L,DD}}^{-1} + \mathbf{R}_{\text{P,DD}}^{-1})\mathbf{G} & \mathbf{G}^T\mathbf{R}_{\text{L,DD}}^{-1}\mathbf{\Lambda} \\ \mathbf{\Lambda}^T\mathbf{R}_{\text{L,DD}}^{-1}\mathbf{G} & \mathbf{\Lambda}^T\mathbf{R}_{\text{L,DD}}^{-1}\mathbf{\Lambda} \end{pmatrix}^{-1} \end{aligned} \quad (35)$$

$$\begin{aligned} \mathcal{F}_{\text{aid}}^{-1} &= \begin{pmatrix} \mathbf{Q}_{\hat{p}\hat{p}} & \mathbf{Q}_{\hat{p}\hat{N}} \\ \mathbf{Q}_{\hat{N}\hat{p}} & \mathbf{Q}_{\hat{N}\hat{N}} \end{pmatrix} \\ &= \begin{pmatrix} \mathbf{G}^T(\mathbf{R}_{\text{L,DD}}^{-1} + \mathbf{R}_{\text{P,DD}}^{-1})\mathbf{G} + H_{5G}^T\mathbf{R}_{5G}^{-1}H_{5G} & \mathbf{G}^T\mathbf{R}_{\text{L,DD}}^{-1}\mathbf{\Lambda} \\ \mathbf{\Lambda}^T\mathbf{R}_{\text{L,DD}}^{-1}\mathbf{G} & \mathbf{\Lambda}^T\mathbf{R}_{\text{L,DD}}^{-1}\mathbf{\Lambda} \end{pmatrix}^{-1} \end{aligned} \quad (36)$$

Lemma 1 elucidates the inequality relationship among the diagonal elements of $\mathbf{Q}_{\hat{p}\hat{p}\text{BDS}}$ and $\mathbf{Q}_{\hat{p}\hat{p}}$.

Lemma 1 For the variance matrix $\mathbf{Q}_{\hat{p}\hat{p}\text{BDS}}$ and $\mathbf{Q}_{\hat{p}\hat{p}}$, the diagonal elements of the former are always less than or equal to those of the latter.

$$[\mathbf{Q}_{\hat{p}\hat{p}}]_{j,j} \leq [\mathbf{Q}_{\hat{p}\hat{p}\text{BDS}}]_{j,j} \quad (37)$$

To characterize the overall position estimation accuracy of BDS/5G RTK positioning in three-dimensional space, a float solution gain factor γ is defined as:

$$\gamma = \sqrt{\frac{[\mathbf{Q}_{\hat{p}\hat{p}\text{BDS}}]_{1,1} + [\mathbf{Q}_{\hat{p}\hat{p}\text{BDS}}]_{2,2} + [\mathbf{Q}_{\hat{p}\hat{p}\text{BDS}}]_{3,3}}{[\mathbf{Q}_{\hat{p}\hat{p}}]_{1,1} + [\mathbf{Q}_{\hat{p}\hat{p}}]_{2,2} + [\mathbf{Q}_{\hat{p}\hat{p}}]_{3,3}}} \geq 1 \quad (38)$$

Compared to BDS only case, BDS/5G RTK positioning exhibits smaller variance in positioning. Additionally, the float solution gain factor is always greater than or equal to 1. This implies that the float solution accuracy of BDS/5G is consistently higher than or equal to that of BDS only case.

Proof The proof of Lemma 1 is in Appendix 1. \square

The calculation of γ requires both the geometric matrix and the auto-covariance matrix of the noise vector. This demonstrates the difference between γ and Position Dilution of Precision (PDOP) can affect γ .

Gains in ADOP

ADOP is a computationally efficient and commonly used metric to evaluate the model strength of ambiguity resolution. The definition of ADOP is as follows:

$$\theta_{\text{ADOP}} = \sqrt{|\mathbf{Q}_{\hat{N}\hat{N}}|}^{\frac{1}{N}} \quad (39)$$

In equation (39), N is the dimension of DD ambiguity, $|\cdot|$ symbol denotes the operation of determinant, and $\mathbf{Q}_{\hat{N}\hat{N}}$ is the variance of float solution. Teunissen (1998) illustrates the relationship between ADOP and the probability of fixing ambiguities successfully:

$$P_c \leq \left[2\Phi\left(\frac{1}{2\theta_{\text{ADOP}}}\right) - 1 \right]^N \quad (40)$$

where $\Phi(\cdot)$ denotes the cumulative distribution function (CDF) of the standard normal distribution.

In equation (35) and (36), the covariance matrix of DD ambiguities can be expanded as:

$$\begin{aligned} \mathbf{Q}_{\hat{N}\hat{N}\text{BDS}} &= \mathbf{\Lambda}^{-1}(\mathbf{R}_{\text{L,DD}}^{-1} + \mathbf{G}^T\mathbf{Q}_{\hat{p}\hat{p}\text{BDS}}\mathbf{G})\mathbf{\Lambda}^{-1} \\ \mathbf{Q}_{\hat{N}\hat{N}} &= \mathbf{\Lambda}^{-1}(\mathbf{R}_{\text{L,DD}}^{-1} + \mathbf{G}^T\mathbf{Q}_{\hat{p}\hat{p}}\mathbf{G})\mathbf{\Lambda}^{-1} \end{aligned} \quad (41)$$

Lemma 2 elucidates the inequality for BDS only and BDS/5G methods.

Lemma 2 The covariance matrix of the DD ambiguities exhibits the following inequality relationship under BDS only case and BDS/5G case:

$$\|\mathbf{Q}_{\hat{N}\hat{N}}\| \leq \|\mathbf{Q}_{\hat{N}\hat{N}\text{BDS}}\| \quad (42)$$

To characterize the improvement in the success rate of ambiguity resolution for BDS/5G solution, the ADOP gain factor η is defined as:

$$\eta = \left(\frac{\sqrt{|\mathbf{Q}_{\hat{N}\hat{N}\text{BDS}}|}}{\sqrt{|\mathbf{Q}_{\hat{N}\hat{N}}|}} \right)^{\frac{1}{N}} \geq 1 \quad (43)$$

The ADOP for BDS/5G solution is always less than or equal to that of BDS only case. Namely, the ADOP gain factor is always greater than or equal to 1, indicating the BDS/5G RTK solution consistently achieves a higher fixing rate.



Fig. 4 Illustration of measurement environment

Proof

The proof of Lemma 2 is in Appendix 2. □

Simulation

In this section, we will compare the proposed method with BDS only method and investigate the influence factors of the proposed method using through numerical simulations of the gain factors in different conditions including 5G measurement accuracy and the number of visible satellites.

Simulation setting

We collected satellite observations to conduct simulation experiments. Figure 4 shows a student dormitory in Tsinghua university. It can be seen that four-wheeled robot is equipped with a GNSS receiver and parked in front of the building, collecting satellite signals.

The skyplot of the rover is shown in Fig. 4. It can be seen that the satellites in the north and northwest are obscured by buildings.

A 5G base station, it is assumed that a 5G base station is located 60 ms to the east at a height of 10 ms higher than the rover. In the simulation, the 5G base station communicated with the rover measuring AoA and RTT.

We will discuss the impact of the number of visible satellites subsequently. To control variables, we have set the standard deviation of the 5G azimuth and zenith AoA measurement noise to 3°, the standard deviation of RTT measurement to 4 ns, and the standard deviation of equivalent RTT ranging noise to 1.2 m. As is illustrated in equation (9), they are independent.

Number of visible satellites

The number of visible satellites will fluctuate with motion trajectory, and therefore the improvement of 5G will also

change accordingly. We explore the positioning performance in the scenes with varying obstruction based on the gain factor defined in the previous section.

In practical environments, the satellites with lower elevation are more susceptible to obstruction of buildings and other objects. Therefore, we use the following principle to simulate the change in visible satellites: for the satellites shown in Fig. 5, we sort them from low to high elevation, and iteratively, the satellite with the lowest elevation will be removed in each step. Then, we calculate the float solution gain factor and ADOP gain factor, as shown in Fig. 6.

Figure 6 shows the curves of float solution factor γ and ADOP gain factor η as the number of satellites changes. The blue dashed line with circle markers represents the curve between γ and the number of visible satellites. And the orange dotted one with triangle markers represents the curve between η and the number of visible satellites. We can see from the Fig. 6 that BDS/5G solution is more pronounced when the number of visible satellites decreases.

When the number of visible satellites is 13, both γ and η approximately reach at 1 and the performance of BDS is already excellent. BDS contributed mainly to positioning result, which is consistent with the weighting method shown in Eq. (9).

When the number of visible satellites gradually decreases to 5, γ increases to 5.6 and η increases to 3.5, which means that the norm of position variance vector is reduced to 1/5.6, and the ADOP is reduced to 1/3.5 compared to BDS only case. This trend means that in urban areas where satellites are severely hindered, using

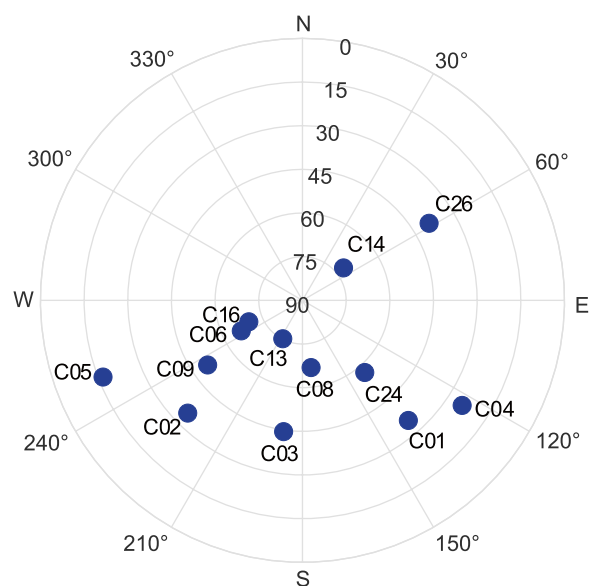


Fig. 5 Skyplot of rover shown in Fig. 4

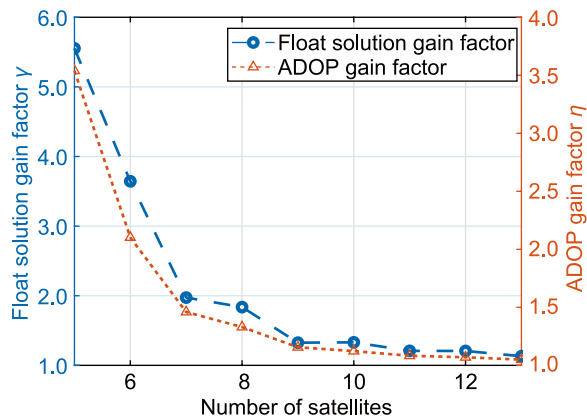


Fig. 6 Relationship between satellite count and gain factors. The blue dashed line with circle markers represents the curve between γ and the number of satellites. And the orange dotted one with triangle markers represents the curve between η and the number of satellites

BDS/5G for positioning can achieve a more significant performance gain in positioning.

Equation (39) shows the relationship between the ADOP and theoretical ambiguity fixing rate. Figure 7 illustrates the correlation between the fixing rate and the number of visible satellites in both the scenarios of BDS only and BDS/5G positioning.

The dashed line marked with a blue circle is for the BDS only case, and the dotted line marked with an orange triangle is for BDS/5G case. When the number of visible satellites is 5, the fixing rate in the BDS only case is 50.3%, while the fixing rate in BDS/5G case is 68.8%. As the number of visible satellites increases, the fixing rate in both cases increases. When the number of visible satellites is greater than 10, the fixing rate is close to 100% in both cases. 5G does not lead to significant improvements due to the excellent performance of BDS only positioning.

Measurement accuracy

In the skyplot shown in Fig. 5, despite some satellites are obstructed by buildings, the visible satellite count still reaches 13. As discussed in Sect. 5.2, the gains from 5G observations are not significant at this point. And this section focuses on the gain obtained by 5G observation in the different accuracy, when the satellite count is set to 6. To simplify the experimental setup, we assume that the observation noise magnitude is consistent for 5G azimuth and zenith AoA observations in this experiment.

Figure 8 illustrates the variation of γ with different 5G measurement accuracies. The horizontal axis represents the angle measurement standard deviation, while the different line styles in the legend indicate RTT ranging standard deviations. A dashed line parallel to the x-axis is

presented in the figure, which means the line $\gamma = 1$. Specifically, when the angle measurement standard deviation is 2° and the ranging standard deviation is 1 m, γ reaches 4, indicating a fourfold performance improvement in the context of float solution accuracy. As the ranging and angle measurement noise increase, the curves gradually approach the dashed line $\gamma = 1$, implying a reduction in the gains introduced by 5G.

The simulation results in Fig. 9 present the correlation between measurement noise and η . With the increasing measurement noise, the curves tend to approach the dashed line $\eta = 1$. When the measurement noise becomes large enough, the curves closely align with the dashed line $\eta = 1$.

Experiment and results analysis

In this section, we used a Huawei 5G CPE to collect AoA measurements in a dynamic environment, operating on a 100 MHz bandwidth centered at 4.9 GHz. During the recording process, we also used a high-precision position reference system to output the position of CPE. Based on the ground truth of CPE and the location of 5G base station, we implement the analysis on the typical error levels of 5G AoA measurements in a dynamic environment.

The robot shown in Fig. 10 is equipped with several sensors including GNSS receiver, LiDAR and IMU. The combination of multi-constellation RTK positioning, INS, and LiDAR is used to obtain the ground truth of the rover.

We selected a reasonable location within the rover's movement area to simulate a 5G base station. Based on the ground truth of the rover and the typical error level of AoA measurement in the dynamic environment, we simulated AoA observations. For RTT, we refer to the current measurement accuracy to set the ranging noise.

We set the data rate of 5G observations at 1 Hz and assume that GNSS and 5G data are synchronized, which can be easily configured in a low dynamic environment. In GNSS and 5G antennas collocation, we assume that GNSS and 5G are in the same phase center after lever adjustment.

Subsequently, we conducted a hybrid positioning experiment by using the BDS measurements collected by the rover and the simulated 5G AoA and RTT measurements. And the hybrid positioning results will be analyzed to evaluate the performance of BDS/5G RTK positioning.

Experiment and results analysis

In this section, we used a Huawei 5G CPE to collect AoA measurements in a dynamic environment, operating on a 100 MHz bandwidth centered at 4.9 GHz.

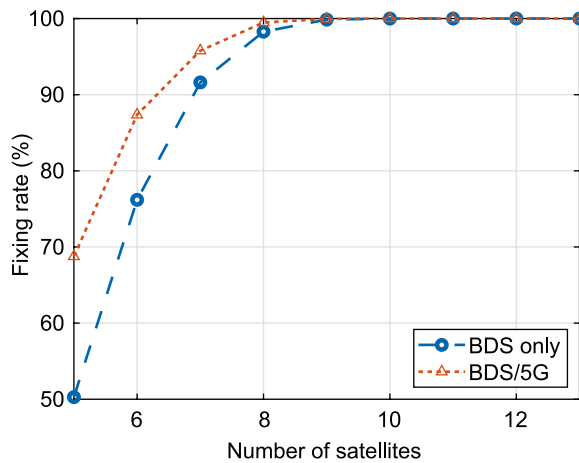


Fig. 7 Curves between the number of visible satellites and ambiguity fixing rate. The blue dashed line with circle markers represents BDS only, while the orange dotted line with triangle markers represents BDS/5G case

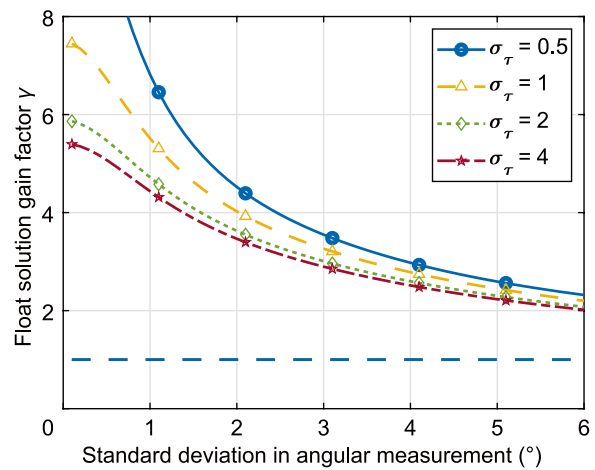


Fig. 8 Effect of 5G measurement noise for float solution gain factor. Different line types are used to differentiate RTT ranging standard deviations. A dashed line parallel to the x-axis is presented in the figure, which means the line $\gamma = 1$

During the recording process, we also used a high-precision position reference system to output the position of CPE. Based on the ground truth of CPE and the location of 5G base station, we implement the analysis on the typical error levels of 5G AoA measurements in a dynamic environment.

The robot shown in Fig. 10 is equipped with sensors including GNSS receiver, LiDAR and IMU. The combination of multi-constellation RTK positioning, INS and LiDAR is used to obtain the ground truth of rover.

We selected a reasonable location within the rover’s movement area to simulate a 5G base station. Based on the ground truth of rover and the typical error level of AoA measurement in the dynamic environment, we generated AoA observations through simulation. For RTT, we refer to the current measurement accuracy to set the ranging noise.

We set the data rate of 5G observation to 1 Hz and assume that GNSS and 5G data are synchronized, which can be easily configured in low dynamic environment. In GNSS and 5G antennas collocation, we assume that GNSS and 5G are in the same phase center after lever adjustment.

Subsequently, we conducted a hybrid positioning experiment by using BDS measurements collected by the rover and the 5G AoA and RTT measurements generated by simulation. And the hybrid positioning results will be analyzed to evaluate the performance of BDS/5G RTK positioning.

BDS measurement collection

On October 20, 2023, data were collected at a sampling frequency of 10 Hz, commencing at 02:22:12, yielding a

total of 3014 epochs. The experiment took place in a tree-shaded environment located between Xinmin Road and the Comprehensive Gymnasium of Tsinghua University, and the rover recorded data in this setting.

Furthermore, a RTK base station was established at the top of Weiqing Building at Tsinghua University to capture BDS observations contemporaneously. The trajectory of the rover is delineated by the arrow in the Fig. 11, while the pentagram denotes the position of the RTK base station.

Both the rover and base station receiver employ a dual-frequency configuration operating in the B1 and B2 frequency bands. In the positioning experiments, we configured the receiver to receive the B1I and B2I signals for BDS2 and the B1I and B2A signals for BDS2 (Fig. 12).

The skyplot of the rover in Fig. 11 is shown in Fig. 12:

Figure 13 shows the change in satellite visibility as the rover moved. We can see variations in the consistency of observations among different satellites. Notably, satellites C08, C13, C14, C28, and C33 consistently provided stable observation. On the other hand, the rest of the satellites exhibited varying degrees of signal flickering, mainly due to the obstructions from tree canopies and buildings. Specifically, satellites C01 and C03 experienced extended interruptions in signal continuity.

During the satellite signal collection process, the receiver sets a satellite cut-off elevation to ensure signal quality. In this experiment, the cut-off elevation is set as 15 degrees.

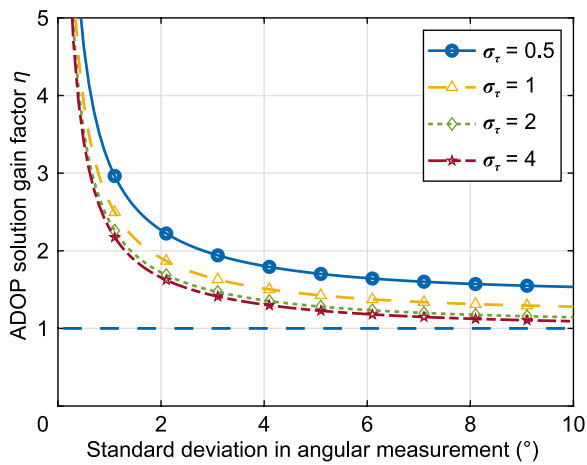


Fig. 9 Effect of 5G measurement noise for ADOP gain factor. Different line types are used to differentiate RTT ranging standard deviations. A dashed line parallel to the x-axis is presented in the figure, which means the line $\eta = 1$

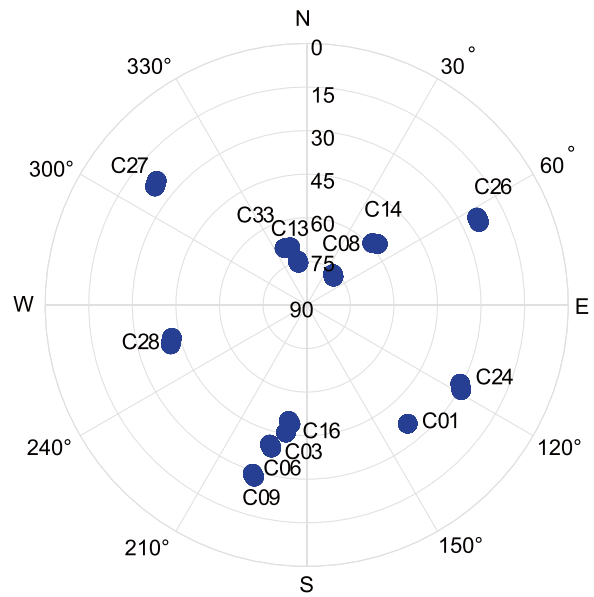


Fig. 12 Skyplot of rover shown in Fig. 11

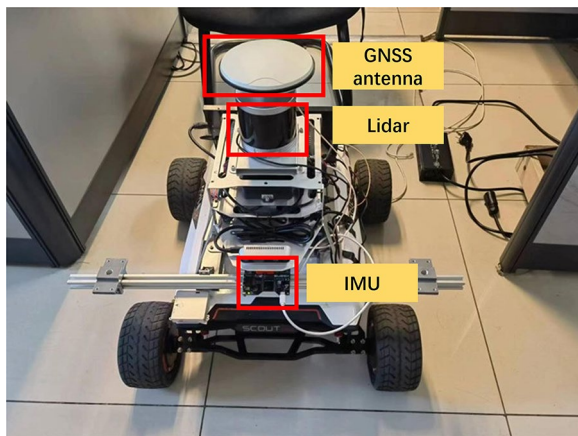


Fig. 10 Entity architecture of experimental equipment

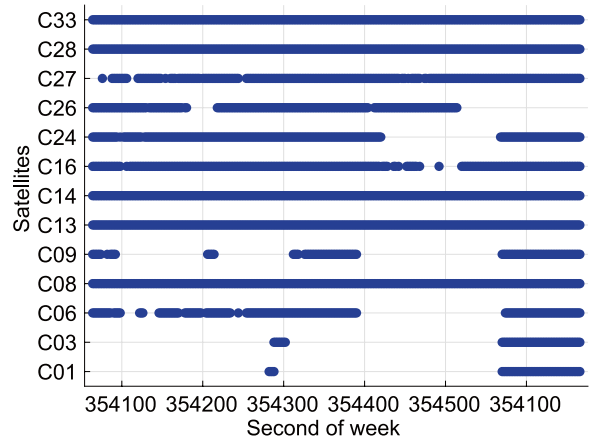


Fig. 13 Visualization of observable satellites in rover shown in Fig. 11



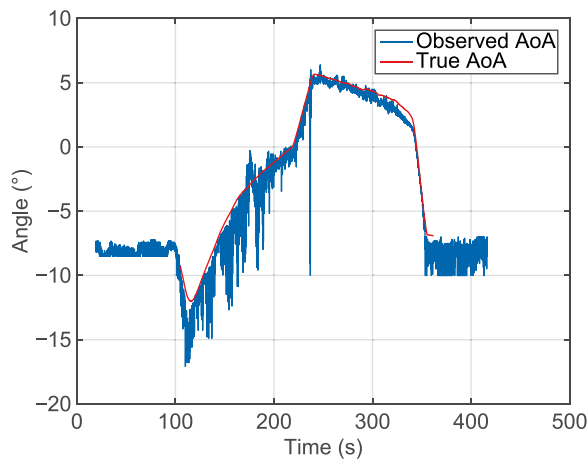
Fig. 11 The illustration of rover and base station generated with Google Earth

5G AoA measurement analysis

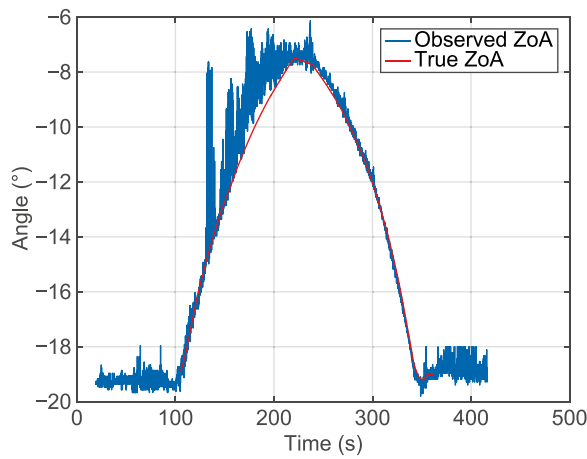
To evaluate the noise in 5G angle measurements, we collected the data in Taicang, Jiangsu, using a CPE



Fig. 14 The illustration of 5G data collection area generated by Baidu Maps



a



b

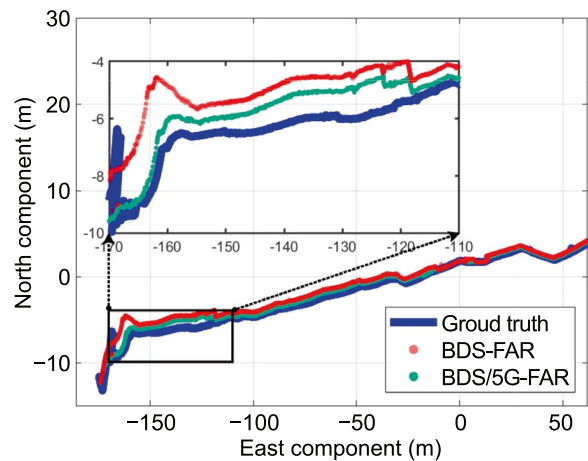
Fig. 15 Comparisons between 5G angle of arrival and ground truth, subfigure (a) depicts comparisons curve of azimuth of angle, and subfigure (b) depicts comparisons curve of zenith of angle

maintained a low dynamic movement. The experiment was conducted in a campus environment with a significant presence of buildings and trees. 5G data collection environment is shown in Fig. 14. The signal received by the CPE is a Line of Sight (LOS) 5G signal with multipath reflections.

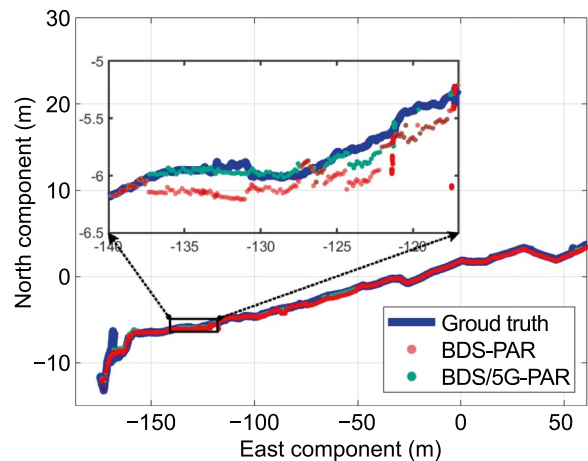
Similar building construction and multipath reflections are present in both the 5G and GNSS data collection environments. Therefore, it is reasonable to generate corresponding 5G AoA observations in the GNSS data collection environment based on the Root Mean Square Error (RMSE) of actual 5G AoA measurements.

The comparison curve between 5G measured AoA and true AoA is depicted in the Fig. 15.

From Fig. 15, most of AoA observations are within the normal range. However, outliers might occur in 5G measurements in more challenging environments. The



a



b

Fig. 16 Trajectories comparison in east-north plane with ground truth, taking the geometric center of the ground truth as the origin, and results of FAR and PAR are shown in subfigure (a) and (b) respectively

design of 5G outlier detection and rejection algorithm is also important. But this is beyond the scope of this paper.

The RMSE for azimuth and zenith AoA are 0.85° and 1.37° respectively. Based on this statistical result, simulations of 5G observations for the rover in Section [BDS measurement collection](#) were conducted. The standard deviations of observational noise for azimuth and zenith AoA were set as $\sigma_\alpha = 0.85^\circ$ and $\sigma_\beta = 1.37^\circ$, respectively, while the standard deviation for RTT measurements was set as 4 ns, corresponding to a distance measurement standard deviation of $\sigma_d = 1.2$ m.

At the geometric center of the rover's motion trajectory, a 5G base station was displaced 60 m eastward, 60 m northward, and 15 m vertically. This setup aimed to simulate AoA and RTT measurements between the rover and the base station to execute a hybrid positioning experiment.

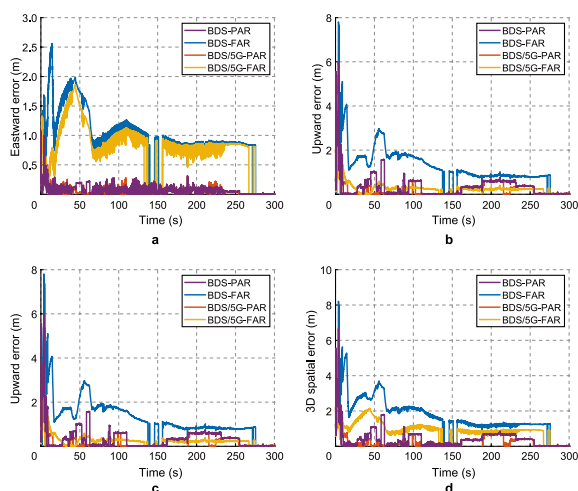


Fig. 17 Positioning error in the eastward, northward, and upward orientations, as well as the overall three-dimensional positioning error, shown in figure (a–d) respectively

Result analysis

To assess the improved performance of BDS/5G RTK positioning, we performed experiments with the dataset.

The robot shown in Fig. 10 is outfitted with an Xsens IMU and a RoboSense 16-beam LiDAR in addition to GNSS. While recording satellite signal, we gathered LiDAR and IMU data concurrently. Then we got the high-precision ground truth with multi-sensor fusion.

We compared the trajectories of the positioning results to the reference trajectory on the East-North plane. The comparative plots can be seen in Fig. 16.

Positioning results

In subfigure (a), achieving a fixed solution with FAR in complicated environment is challenging, and the positioning of the BDS-FAR exhibits a notable deviation at the initial phase of positioning. However, the trajectory of BDS/5G method aligns more closely with the ground truth. Moving to subfigure (b), the deviation of the positioning scatter points from the ground truth in the magnified area exhibits discontinuity, where the scatter points consistently deviate from the ground truth starting from

a specific point, and then experience another abrupt jump after a period of time. This discrete jump is a result of the integer nature of the error in ambiguity subset resolution. In this context, the utilization of the PAR method is observed to mitigate the positioning error inherent in RTK positioning. In this scenario, the trajectories of BDS only and BDS/5G converge more closely to the ground truth. However, it is notable that certain scattered points in the trajectory of BDS only positioning significantly deviate from the ground truth, whereas the trajectory of BDS/5G positioning demonstrates greater stability and accuracy.

Figure 17 illustrates the positional errors in the eastward, northward, upward axes directions, along with the three-dimensional spatial positioning errors.

From Fig. 17, the error curve in the FAR mode abruptly decreases around an observation time of 150 s, indicating a transition from float solution to fixed solution. After the successful ambiguity resolution, the error decreases sharply, and the points with positioning errors exceeding the centimeter level are classified from float solutions. The figure demonstrates the significant accuracy gain of BDS/5G RTK positioning for float solutions. In each subfigure, BDS/5G-FAR is consistently positioned below BDS-FAR, indicating higher accuracy throughout. The error reduction is most significant in the upward orientation in subfigure (c).

In the PAR mode, noticeable reductions in errors are observed across each axis and in three-dimensional space when compared to the FAR mode. In the BDS-PAR mode, there are pulse-like increases in errors occurring approximately at 50 s and 100 s, attributable to the errors in ambiguity resolution. Conversely, the error curve for the BDS/5G-PAR configuration maintains a consistently stable trajectory without such notable fluctuations.

Error statistics

Table 1 depicts the fixing rate and the positioning RMSE within the dataset with the employing BDS only, 5G and BDS/5G methods. In the this scenario, BDS positioning demonstrates better performance than

Table 1 Table of positioning results statistics

	Method	Fixing rate (%)	RMSE (m)			
			East	North	Up	3D
FAR	BDS	11.11	1.04	0.74	1.54	2.00
	BDS/5G	13.93	0.86	0.43	0.40	1.04
PAR	BDS	32.58	0.12	0.27	0.63	0.69
	BDS/5G	44.43	0.12	0.22	0.51	0.56
	5G	–	1.70	2.44	2.68	4.00

5G positioning. In the BDS-FAR mode, the 3D RMSE is 2 m for BDS compared to 4 m for 5G. Furthermore, upon further observation, the fusion of BDS and 5G systems has led to an improvement in the RTK positioning performance. In the case of fixed epoch statistics, the epochs with a positioning error exceeding 10 cm are excluded. We consider only the epochs that have achieved centimeter-level accuracy and successful ambiguity resolution as fixed epochs. In the FAR mode, the fixing rate for BDS only method is 11.11%, and 13.93% when augmented with 5G measurements. Concurrently, the spatial positioning RMSE is reduced from 2 m to 1.04 m, indicating 48% reduction in error. In the PAR mode, the fixing rate rises from 32.58% to 44.43% with the incorporation of 5G measurement, but spatial positioning RMSE is reduced from 0.69 m to 0.56 m, an 18.84% reduction.

In Fig. 17, it is apparent that the filter undergoes pronounced error with oscillations during the initial period. Within the initial 10 s, the filter converges resulting in a significant reduction in error. To conduct a more detailed comparative analysis of the distribution of positioning errors across different modes, a 3D spatial positioning error box plot was generated after convergence of the filter in the Fig. 18.

In the FAR mode, the median of the positioning error for BDS only method exceeds 1 m, and the third quartile surpasses 2 m. Additionally, a substantial number of outliers are present in this dataset, with positioning errors potentially exceeding 5 m. In terms of BDS/5G method, the median positioning error is less than 1 m, with a decline in the third quartile to 1.05 m. In this mode, the boxplot exhibits a flattened shape, indicating a concentration of errors around 1 m. There is a notable improvement in outliers, and fixed epochs are represented as

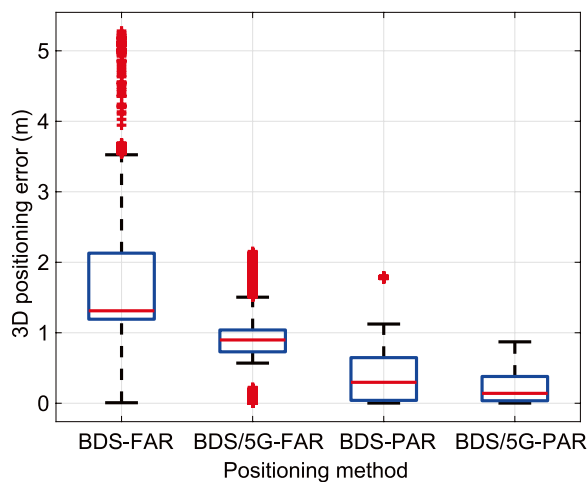


Fig. 18 Boxplot of positioning errors

scattered points below the box, considered as deviations from the data center.

In the PAR mode, there is a noticeable improvement in positioning errors compared to FAR. For the BDS only method, the median error is 0.5m, and the third quartile error is 0.65 m. However, a few outliers persist, with errors ranging between 1 m and 2 m. In the BDS/5G method, the median error is 0.12 m, and the third quartile error is 0.38 m, without occurrence of outliers, which highlights the enhancement to 5G-assisted BDS RTK positioning.

Fig. 19 presents the CDF curves of 3D positioning errors for various positioning methods. For 5G positioning, its CDF curve shows a gradual increase due to the assumption of Gaussian white noise in the measurement noise. In the FAR mode, a significant discontinuity in the CDF curve can be observed. This discontinuity represents the transition between float solutions and fixed solutions. When the FAR mode can achieve the correct fixed solution, centimeter-level positioning accuracy is often obtained. Comparing the BDS-FAR and BDS/5G-FAR curves, we can see that in the FAR mode, the gain of 5G in RTK positioning mainly manifests in the improvement of float solution. The PAR mode exhibits a smoother change in the curve compared to the FAR mode. PAR mode is more tolerant towards ambiguity resolution compared to the FAR. PAR mode only requires a subset of the ambiguities to be resolved, although this may increase the probability of ambiguity fixing errors, the processing of partial subsets can still yield overall positioning accuracy gains, especially in complicated environment. In Fig. 19, the curves of BDS-PAR and BDS/5G-PAR show that 5G

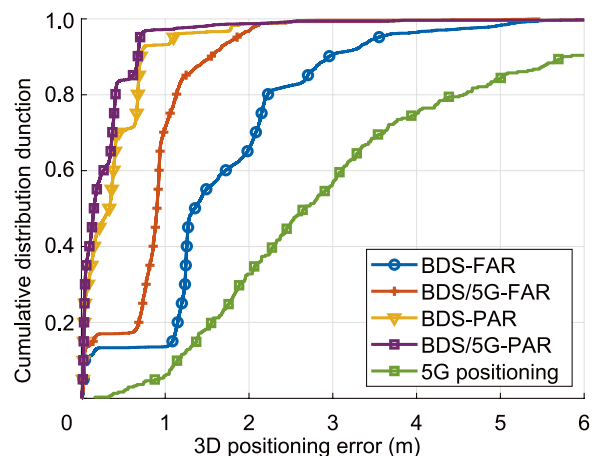


Fig. 19 Cumulative distribution curve of the positioning results. Different colors and markers on the curve are used to differentiate between different positioning modes

assistance can reduce errors in fixing ambiguity subset under the PAR mode.

Conclusions

This paper proposes a method for 5G-assisted BDS RTK positioning, which utilizes AoA and RTT observations in 5G system to assist BDS RTK positioning, to obtain more accurate float solution and a higher ambiguity fixing rate.

We derive the CRLB for the BDS/5G method and prove the inequality between the CRLB of BDS only and BDS/5G methods. This mathematically proves the performance improvement with 5G observations in RTK positioning. Based on this, we further propose the float solution gain factor and ADOP gain factor to characterize the performance gain of 5G observations in RTK positioning. The float solution gain factor intuitively reflects the improvement of the variance of rover position, and ADOP gain factor indicates how 5G observations improve the estimation accuracy of ambiguities. Furthermore, we indicate the variation of the float solution gain factor and ADOP gain factor under different 5G measurement accuracy and visible satellite numbers using simulation. The gain factors in simulation results indicate a significant improvement in the RTK float solution estimation and ambiguity fixing rate in urban environment with the current 5G measurement accuracy.

In the experiment, we analyze the noise of observations based on 5G field test data and combine it with actual BDS measurements for positioning experiments. The results verify the improvement of the proposed method in positioning performance in complex environments. The experimental results show that 5G-assisted BDS RTK has a certain improvement effect on the overall positioning error in both FAR and PAR modes. Additionally, it can reduce the occurrence of outliers, achieving more accurate and robust positioning.

In future, we plan to seek potential support from network operators to explore the performance benefits of BDS/5G in diverse real-world scenarios. Furthermore, we will further explore outlier detection and integrity enhancement in positioning using BDS/5G measurements.

Appendix 1 Derivation of Lemma 1

The expression for the covariance matrix pertaining to the estimation of the receiver position in a float solution can be derived using the matrix inversion formula as presented in equation (35) and (36).

$$\begin{aligned} \mathbf{Q}_{\hat{p}\hat{p}_{\text{BDS}}} &= \left[\mathbf{G}^T (\mathbf{R}_{L,DD}^{-1} + \mathbf{R}_{P,DD}^{-1}) \mathbf{G} - \mathbf{G}^T \mathbf{R}_{L,DD}^{-1} \mathbf{G} \right]^{-1} \\ &= (\mathbf{G}^T \mathbf{R}_{P,DD}^{-1} \mathbf{G})^{-1} \\ \mathbf{Q}_{\hat{p}\hat{p}} &= (\mathbf{G}^T \mathbf{R}_{P,DD}^{-1} \mathbf{G} + \mathbf{H}_{5G}^T \mathbf{R}_{5G}^{-1} \mathbf{H}_{5G})^{-1} \end{aligned} \tag{A.1}$$

Let $\mathcal{F} = \mathbf{G}^T \mathbf{R}_{P,DD}^{-1} \mathbf{G}$. Employing the Woodbury matrix inversion formula, we expand this expression as follows:

$$\begin{aligned} \mathbf{Q}_{\hat{p}\hat{p}_{\text{BDS}}} &= \mathcal{F}^{-1} \\ \mathbf{Q}_{\hat{p}\hat{p}} &= \mathcal{F}_1^{-1} - \mathcal{F}_1^{-1} \mathbf{H}_{5G}^T (\mathbf{R}_{5G} + \mathbf{H}_{5G} \mathcal{F}_1^{-1} \mathbf{H}_{5G}^T)^{-1} \mathbf{H}_{5G} \mathcal{F}_1^{-1} \end{aligned} \tag{A.2}$$

The disparity between two covariance matrices is expressed as:

$$\mathbf{X} = \mathbf{Q}_{\hat{p}\hat{p}} - \mathbf{Q}_{\hat{p}\hat{p}_{\text{BDS}}} \tag{A.3}$$

$$= \mathcal{F}_1^{-1} \mathbf{H}_{5G}^T (\mathbf{R}_{5G} + \mathbf{H}_{5G} \mathcal{F}_1^{-1} \mathbf{H}_{5G}^T)^{-1} \mathbf{H}_{5G} \mathcal{F}_1^{-1} \tag{A.4}$$

\mathcal{F}_1^{-1} is a positive semi-definite matrix, therefore matrix $\mathbf{H}_{5G} \mathcal{F}_1^{-1} \mathbf{H}_{5G}^T$ is also positive semi-definite. And a matrix decomposition will be conducted on $\mathbf{H}_{5G} \mathcal{F}_1^{-1} \mathbf{H}_{5G}^T$:

$$\mathbf{H}_{5G} \mathcal{F}_1^{-1} \mathbf{H}_{5G}^T = \mathbf{Q}_2^T \mathbf{\Lambda}_2 \mathbf{Q}_2 \tag{A.5}$$

Substituting (A.5) into (A.3), the following equation holds:

$$\mathbf{X} = \mathcal{F}_1^{-1} \mathbf{H}_{5G}^T \mathbf{Q}_2^T (\mathbf{R}_{5G} + \mathbf{\Lambda}_2)^{-1} \mathbf{Q}_2 \mathbf{H}_{5G} \mathcal{F}_1^{-1} \tag{A.6}$$

In order to facilitate the simplification of the preceding expression, introduce the notation $\mathbf{T} = \mathcal{F}_1^{-1} \mathbf{H}_{5G}^T \mathbf{Q}_2^T$, $\mathbf{\Lambda}_3 = (\mathbf{R}_{5G} + \mathbf{\Lambda}_2)^{-1}$ is a positive semi-definite matrix. Consequently, the expression can be decomposed as:

$$\mathbf{X} = \mathbf{T}^T \mathbf{\Lambda}_3 \mathbf{T} \tag{A.7}$$

From the structure of $\mathbf{\Lambda}_3$, it is evident that it is a diagonal positive definite matrix. Due to the relationship between \mathbf{X} and $\mathbf{\Lambda}_3$, the matrix \mathbf{X} can be expressed in the following form:

$$\mathbf{X} = \sum_{j=1}^N \lambda_{x,j} \mathbf{t}_{x,j}^T \mathbf{t}_{x,j} \tag{A.8}$$

Here, $\lambda_{x,j}$ is the j -th element of the diagonal matrix $\mathbf{\Lambda}_3$, $\mathbf{t}_{x,j}$ is the j -th row vector of \mathbf{T} , and N is the dimension of the matrix \mathbf{X} . $\mathbf{t}_{x,j}^T \mathbf{t}_{x,j}$ is a positive semi-definite matrix, and $\lambda_{x,j} \geq 0$. Therefore, we can conclude:

$$[\mathbf{X}]_{i,i} \geq 0 \tag{A.9}$$

This leads to the following inequality:

$$[\mathbf{Q}_{\hat{p}\hat{p}}]_{i,i} \leq [\mathbf{Q}_{\hat{p}\hat{p}BDS}]_{i,i} \quad (\text{A.10})$$

Appendix 2 Derivation of Lemma 2

Regarding the ambiguity covariance matrices $\mathbf{Q}_{\hat{N}\hat{N}BDS}$ and $\mathbf{Q}_{\hat{N}\hat{N}}$, their respective expressions, as outlined in equation (41), primarily diverge in the middle term within the brackets. To deliberate upon the inequality relationship of determinants, \mathbf{M}_1 and \mathbf{M}_2 are denoted as:

$$\begin{aligned} \mathbf{M}_1 &= (\mathbf{R}_{L,DD}^{-1} + \mathbf{G}^T \mathbf{Q}_{\hat{p}\hat{p}BDS} \mathbf{G}) \\ \mathbf{M}_2 &= (\mathbf{R}_{L,DD}^{-1} + \mathbf{G}^T \mathbf{Q}_{\hat{p}\hat{p}} \mathbf{G}) \end{aligned} \quad (\text{B.11})$$

Substituting the specific expressions (A.2) and (A.3) for $\hat{p}\hat{p}BDS$ and $\mathbf{Q}_{\hat{p}\hat{p}BDS}$, we obtain:

$$\begin{aligned} \mathbf{M}_1 &= \mathbf{R}_{L,DD}^{-1} + \mathbf{G}^T \mathcal{F}_1^{-1} \mathbf{G} \\ \mathbf{M}_2 &= \mathbf{R}_{L,DD}^{-1} + \mathbf{G}^T \mathcal{F}_1^{-1} \mathbf{G} - \mathbf{G}^T \mathbf{X} \mathbf{G} \end{aligned} \quad (\text{B.12})$$

Let $\mathbf{M}_3 = \mathbf{G}^T \mathbf{X} \mathbf{G}$, then $\mathbf{M}_2 = \mathbf{M}_1 - \mathbf{M}_3$. Regarding the matrix \mathbf{M}_1 , $\lambda_k(\mathbf{M}_1)$ signifies the k -th eigenvalue of \mathbf{M}_1 , arranged in ascending order ($k = 1, \dots, M-1$). Both \mathbf{M}_1 and $-\mathbf{M}_3$ represent instances of Hermitian matrices within the realm of real symmetric matrices. In accordance with the Weyl inequality, for any k ,

$$\lambda_k(\mathbf{M}_1 - \mathbf{M}_3) \leq \lambda_k(\mathbf{M}_1) + \lambda_n(-\mathbf{M}_3) \quad (\text{B.13})$$

\mathbf{X} is a positive semi-definite matrix, and we can reach that $\lambda_n(-\mathbf{M}_3) \leq 0$, thus:

$$\lambda_k(\mathbf{M}_2) = \lambda_k(\mathbf{M}_1 - \mathbf{M}_3) \leq \lambda_k(\mathbf{M}_1) \quad (\text{B.14})$$

This substantiates the augmentation in the ADOP coefficient, demonstrated by the validity of the following inequality:

$$\begin{aligned} \|\mathbf{M}_2\| &\leq \|\mathbf{M}_1\| \\ \|\mathbf{Q}_{\hat{N}\hat{N}}\| &\leq \|\mathbf{Q}_{\hat{N}\hat{N}BDS}\| \end{aligned} \quad (\text{B.15})$$

Abbreviations

RTK	Real-time kinematic
ADOP	Ambiguity dilution of precision
BDS	BeiDou navigation satellite system
FAR	Full ambiguity resolution
PAR	Partial ambiguity resolution
GNSS	Global navigation satellite system
IoT	Internet of things
UWB	Ultra-wideband
CID	Cell identity
AoA	Angle of arrival
AoD	Angle of departure
SNR	Signal-to-noise rate
TOA	Time of arrival
TDOA	Time of difference of arrival

RTT	Round trip time
MIMO	Multiple-input multiple output
EKF	Extended Kalman filter
LAMBDA	Least-squares ambiguity decorrelation adjustment
CPE	Customer premises equipment
DD	Double difference
CRLB	Cramer–Rao lower bound
CDF	Cumulative distribution function

Acknowledgements

We would express our sincere gratitude to Dr. Caoming Fan for his guidance and advice in GNSS data processing, and to Dr. Gang Liu for his suggestions and assistance in the application of experimental equipment.

Author contributions

Weixiang Chen contributed to the methodology and writing of the manuscript. Tengfei Wang provided supervision, project administration, conceived this study and funding acquisition. Mingquan Lu and Zhen Yao contributed to the review and editing process. Yi Wang and Cheng Li provided the data collection and analysis on 5G system. All authors have thoroughly reviewed and approved the final manuscript.

Funding

This work was supported by the National Key R&D Program of China under Grant No. 2021YFA0716603 and the 6th Young Elite Scientist Sponsorship Program through the China Association for Science and Technology under Grant YESS20200226.

Availability of data and materials

The GNSS datasets used for simulation in section [Experiment and results analysis](#) and positioning experiment in section [Experiment and results analysis](#) are available from github repository (<https://github.com/chenwx63/DataCollection20231019.git>). The 5G datasets are not publicly available due to the cooperation agreement with Huawei but are available from the corresponding author on reasonable request.

Declarations

Competing interests

The authors declare that they have no known competing financial interests or personal relationships that could have influenced the work reported in this study.

Received: 4 January 2024 Accepted: 13 June 2024

Published online: 26 August 2024

References

- Abu-Shaban, Z., Seco-Granados, G., Benson, C.R., & Wymeersch, H. (2020). Performance analysis for autonomous vehicle 5g-Assisted positioning in GNSS-Challenged environments. *2020 IEEE/ION position, location and navigation symposium (PLANS)* (pp. 996–1003).
- Bai, L., Sun, C., Dempster, A. G., Zhao, H., Cheong, J. W., & Feng, W. (2022). GNSS-5G hybrid positioning based on multi-rate measurements fusion and proactive measurement uncertainty prediction. *IEEE Transactions on Instrumentation and Measurement*, *71*, 1–15. <https://doi.org/10.1109/TIM.2022.3154821>
- Bai, X., Wen, W., & Hsu, L.-T. (2020). Using Sky-pointing fish-eye camera and LiDAR to aid GNSS single-point positioning in urban canyons. *IET Intelligent Transport Systems*, *14*(8), 908–914. <https://doi.org/10.1049/iet-its.2019.0587>
- Castro-Arvizu, J. M., Medina, D., Ziebold, R., Vilà-Valls, J., Chaumette, E., & Closas, P. (2021). Precision-aided partial ambiguity resolution scheme for instantaneous RTK positioning. *Remote Sensing*, *13*(15), 2904. <https://doi.org/10.3390/rs13152904>
- Chen, K., Chang, G., & Chen, C. (2021). Ginav: A matlab-based software for the data processing and analysis of a gnss/ins integrated navigation system. *GPS Solutions*, *25*(3), 1–7.

- Del Peral-Rosado, J. A., Gunnarsson, F., Dwivedi, S., Razavi, S. M., Renaudin, O., López-Salcedo, J. A., & Seco-Granados, G. (2020). Exploitation of 3d city maps for hybrid 5g rtt and gnss positioning simulations. *Icassp 2020–2020 IEEE international conference on acoustics, speech and signal processing (icassp)* (pp. 9205–9209).
- Del Peral-Rosado, J. A., Saloranta, J., Destino, G., López-Salcedo, J. A., & Seco-Granados, G. (2018). Methodology for simulating 5G and GNSS high-accuracy positioning. *Sensors*. <https://doi.org/10.3390/s18103220>
- Deng, Z., Zheng, X., Zhang, C., Wang, H., Yin, L., & Liu, W. (2020). A TDOA and PDR fusion method for 5G indoor localization based on virtual base stations in unknown areas. *IEEE Access*, 8, 225123–225133. <https://doi.org/10.1109/ACCESS.2020.3044812>
- Destino, G., Saloranta, J., Seco-Granados, G., & Wymeersch, H. (2018). Performance analysis of hybrid 5G-GNSS localization. *2018 52nd asilomar conference on signals, systems, and computers* (pp. 8–12).
- Henkel, P., & Günther, C. (2010). Partial integer decorrelation: Optimum trade-off between variance reduction and bias amplification. *Journal of Geodesy*, 84, 51–63.
- Keating, R., Säily, M., Hulkkonen, J., & Karjalainen, J. (2019). Overview of positioning in 5G new radio. In *2019 16th international symposium on wireless communication systems (ISWCS)* (pp. 320–324).
- King, R. (1995). Documentation for the gamit gps analysis software. *Mass. Inst. of Technol.*
- Li, B., Shen, Y., Feng, Y., Gao, W., & Yang, L. (2014). GNSS ambiguity resolution with controllable failure rate for long baseline network RTK. *Journal of Geodesy*, 88(2), 99–112.
- Li, D., Chu, X., Wang, L., Lu, Z., Zhou, S., & Wen, X. (2022). Performance evaluation of E-CID based positioning on OAI 5G-NR testbed. In *2022 IEEE/CIC international conference on communications in china (ICCC)* (pp. 832–837).
- Li, F., Tu, R., Han, J., Zhang, S., Liu, M., & Lu, X. (2023). Performance research of real-time kinematic/5G combined positioning model. *Measurement Science and Technology*, 34(3), 035115. <https://doi.org/10.1088/1361-6501/aca8c3>
- Li, F., Tu, R., Hong, J., Zhang, S., Zhang, P., & Lu, X. (2022). Combined positioning algorithm based on BeiDou navigation satellite system and raw 5G observations. *Measurement*, 190, 110763. <https://doi.org/10.1016/j.measurement.2022.110763>
- Liu, S., Zhang, L., & Li, J. (2016). A dual frequency carrier phase error difference checking algorithm for the GNSS compass. *Sensors*, 16(12), 1988.
- Medina, D., Li, H., Vilà-Valls, J., & Closas, P. (2021). Robust filtering techniques for RTK positioning in harsh propagation environments. *Sensors (Basel)*, 21(4), 1250. <https://doi.org/10.3390/s2104125033578725>
- Moradbeikie, A., Keshavarz, A., Rostami, H., Paiva, S., & Lopes, S. I. (2021). GNSS-Free outdoor localization techniques for resourceconstrained IoT architectures: A literature review. *Applied Sciences*, 11, 10793. <https://doi.org/10.3390/app112210793>
- Pan, M., Liu, P., Liu, S., Qi, W., Huang, Y., You, X., & Li, X. (2022). Efficient joint DOA and TOA estimation for indoor positioning with 5G picocell base stations. *IEEE Transactions on Instrumentation and Measurement*, 71, 1–19.
- Parkins, A. (2011). Increasing GNSS RTK availability with a new single-epoch batch partial ambiguity resolution algorithm. *GPS Solutions*, 15, 391–402.
- Shahmansoori, A., Garcia, G. E., Destino, G., Seco-Granados, G., & Wymeersch, H. (2018). Position and orientation estimation through millimeter-wave MIMO in 5G systems. *IEEE Transactions on Wireless Communications*, 17(3), 1822–1835. <https://doi.org/10.1109/TWC.2017.2785788>
- Takasu, T. (2013). RTKLIB ver. 2.4. 2 manual. *RTKLIB: An Open Source Program Package for GNSS Positioning*, 29, 49.
- Takikawa, K., Atsumi, Y., Takanose, A., & Meguro, J. (2021). Vehicular trajectory estimation utilizing slip angle based on GNSS Doppler/IMU. *ROBOMECH Journal*, 8(1), 5. <https://doi.org/10.1186/s40648-021-00195-4>
- Teunissen, P. (1993). Least-Squares Estimation of the Integer GPS Ambiguities. Teunissen, P. J., & Odijk, D. (1997). Ambiguity dilution of precision: Definition, properties and application. In *Proceedings of the 10th international technical meeting of the satellite division of the institute of navigation (ion gps 1997)* (pp. 891–899).
- Teunissen, P. J. G. (1998). Success probability of integer GPS ambiguity rounding and bootstrapping. *Journal of Geodesy*, 72(10), 606–612. <https://doi.org/10.1007/s001900050199>
- Teunissen, P. J. G., Joosten, P., & Tiberius, C. C. J. M. (1999). Geometry-free ambiguity success rates in case of partial fixing. In *Proceedings of the national technical meeting of the institute of navigation* (pp. 825–829).
- Wang, C., Xi, J., Xia, C., Xu, C., & Duan, Y. (2023). Indoor fingerprint positioning method based on real 5G signals. In *Proceedings of the 2023 7th international conference on machine learning and soft computing* (pp. 205–210).
- Wang, Y., Zhao, B., Zhang, W., & Li, K. (2022). Simulation experiment and analysis of GNSS/INS/LEO/5G integrated navigation based on federated filtering algorithm. *Sensors*, 22, 550. <https://doi.org/10.3390/s22020550>
- Khafa, A., Del Peral-Rosado, J. A., López-Salcedo, J. A., & Seco-Granados, G. (2021). Evaluation of 5G positioning performance based on UTDoA, AoA and base-station selective exclusion. *Sensors*, 22(1), 101. <https://doi.org/10.3390/s22010101>
- Xie, G. (2009). Principles of GPS and receiver design. *Principles of GPS and receiver design*.
- Yu, K., Rizos, C., Dempster, D., Dempster, A. G., Zhang, K., & Markgraf, M. (2014). An overview of GNSS remote sensing. *EURASIP Journal on Advances in Signal Processing*, 2014(1), 134. <https://doi.org/10.1186/1687-6180-2014-134>
- Zangenehnejad, F., & Gao, Y. (2021). GNSS smartphones positioning: Advances, challenges, opportunities, and future perspectives. *Satellite Navigation*, 2(1), 24. <https://doi.org/10.1186/s43020-021-00054-y>
- Zhao, W., Liu, G., Gao, M., Zhang, B., Hu, S., & Lyu, M. (2023). A new inter-system double-difference RTK model applicable to both overlapping and non-overlapping signal frequencies. *Satellite Navigation*, 4(1), 22.
- Zheng, P., Liu, X., Ballal, T., & Al-Naffouri, T. Y. (2023). 5G-Aided RTK Positioning in GNSS-Deprived Environments.

Publisher's Note

Springer Nature remains neutral with regard to jurisdictional claims in published maps and institutional affiliations.